A Low-power Impedance-to-frequency Converter for Frequency-Multiplexed Wearable Sensors

Weilun Li *Graduate Student Member, IEEE*, Junyi Zhao, Yong Wang *Member, IEEE*, Chuan Wang, and Shantanu Chakrabartty, *Senior Member, IEEE*

***Abstract*— We propose a low-power impedance-to-frequency (I-to-F) converter for wearable transducers that change both its resistance and capacitance in response to mechanical deformation or changes in ambient pressure. At the core of the proposed I-to-F converter is a fixed-point circuit comprising of a voltage-controlled relaxation oscillator and a proportional-to-temperature (PTAT) current reference that locks the oscillation frequency according to the impedance of the transducer. Using both analytical and measurement results we show that the operation of the proposed I-to-F converter is well matched to a specific class of sponge mechanical transducer where the system can achieve higher sensitivity when compared to a simple resistance measurement techniques. Furthermore, the oscillation frequency of the converter can be programmed to ensure that multiple transducer and I-to-F converters can communicate simultaneously over a shared channel (physical wire or virtual wireless channel) using frequency-division multiplexing. Measured results from proof-of-concept prototypes show an impedance sensitivity of 19.66 Hz/Ω at 1.1 kΩ load impedance magnitude and a current consumption of 128 µA. As a demonstration we show the application of the I-to-F converter for human gesture recognition and for radial pulse sensing.**

***Index Terms*— Impedance-to-frequency converter, multimodal sensors, Frequency multiplexing, Wearable sensor, Strain gauge sensor**

I. Introduction

SMART wearable sensors have gained considerable attention in several fields that include human health monitoring, human-machine interface, and motion detection [3]–[11]. These soft and flexible sensors can be comfortably and securely attached to the human body surface while converting physical signals into electrical signals. However, in traditional wearable sensors for detecting variations in strain or pressure, the transduction mechanism involves a change in only one of their electrical properties, its resistance or its capacitance, in response to an external mechanical stimulus [12]–[17]. In this regard, we recently reported a wearable sponge transducer [1], [2] that can produce changes in both resistance and capacitance in response to the external mechanical stimulus. Fig. 1(a) illustrates the cross-sectional view of the poly(3,4-ethylene dioxythiophene) polystyrene sulfonate (PEDOT:PSS) sponge transducer reported in [1] where the air gaps within the transducer contribute towards the total capacitance C_L measured

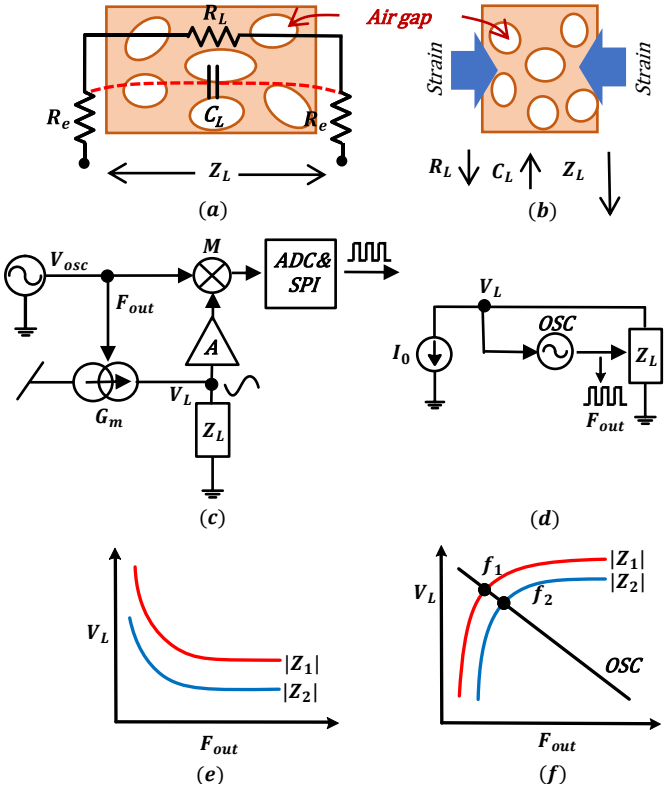

Fig. 1. (a) Cross-sectional illustration of a sponge transducer [1], [2] comprising of several air-gaps which contribute to the transducer capacitance; (b) mechanical deformation of the transducer leads to change in resistance and capacitance; (c)-(e) A conventional approach for measuring changes in impedance; and (d)-(f) proposed approach using a fixed-point frequency locking technique

This work was supported by grants from the Bill & Melinda Gates Foundation (INV-037302) and by a grant from NIH/Eunice Kennedy Shriver National Institute of Child Health and Human Development (R01HD105905). This work involved human subjects in its research. Approval of all ethical and experimental procedures and protocols was granted by the Washington University in St. Louis Institutional Review Board Under Application No.201907109

Weilun Li, Junyi Zhao, Chuan Wang, and Shantanu Chakrabartty, are with the Department of Electrical and Systems Engineering at Washington University in St. Louis, St. Louis, MO 63130 USA. Yong Wang is with the Department of Obstetrics and Gynecology at the Washington University in St. Louis, St. Louis, MO 63130 USA. All correspondences regarding this manuscript should be addressed to *shantanu@wustl.edu*.

across the transducer. The resistance across the transducer R_L on the other hand is determined by the density of the conductive polymer PEDOT:PSS. When the transducer is subjected to a mechanical strain, as shown in Fig. 1(b) both the resistance and capacitance change but in opposite directions respectively. This implies that an impedance measurement method that weighs the change in R_L and C_L appropriately (opposite sensitivity) can achieve significantly higher sensitivity than just measuring the resistance or the capacitance alone. Another challenge in scaling the number of wearable/flexible sensors is that each of the sensor units needs to be ultra-low-power and each sensor can be individually addressed so that the information can be retrieved. In a conventional implementation, the information is multiplexed on a physical (wire or body) channel [18]–[21] or a virtual (packet-switched) channel [22]–[24]. This requires the integration of batteries on the sensor or the use of remote powering, both of which require ultra-low-power impedance sensing and communication circuits.

In literature, the most common approach for measuring impedance follows a topology shown in Figure 1(c) [25]–[29]. A voltage controlled current source G_m, drives the sensor impedance Z_L resulting in a voltage V_L across the sensor. V_L is then demodulated by M using the source signal V_{OSC} as a reference. Using both coherent and non-coherent approaches the impedance can be measured at different frequencies F_{out} as shown in Figure 1(e). Generally, the frequency at which the impedance is measured F_{out} is chosen a-priori or swept over a pre-determined range; however, the optimal operating frequency could vary based on the sensor dimensions and the environmental conditions (sweat and dry conditions). Also, to minimize the power dissipation and for safety considerations, the impedance Z_L is driven using small currents, hence an amplifier is required to amplify the change in voltage V_L. An Analog-to-digital converter (ADC) and serial peripheral interface (SPI) interfaces are used for extracting the impedance changes and for signal transmission and post-processing. However, if the objective is to measure the change in the magnitude of the impedance $|Z_L|$ rather than its resistive or reactive components, then the number of modules (and hence power) can be significantly reduced. Also, note that the conventional approach shown 1(e) uses an open-loop configuration, implying that any noise injected into the internal nodes has to compensated using post-processing techniques.

In this paper, we explore a compact, low-power impedance-to-frequency (I-to-F) converter shown in Fig. 1(d) and alleviates some of the disadvantages of the topology shown in Fig. 1(c). It uses a current reference source and a voltage-controlled oscillator (VCO) in a feedback configuration to modulate the sensor's impedance (due to its resistive & capacitive elements). The configuration thus locks the frequency F_{out} such that the average current I_0 driven through the sensor impedance remains constant. This is equivalent to a transfer characteristic shown in Fig 1(f) where the fixed-point (V_L, F_{out}) is determined by the sensor impedance Z_L. The key advantages of the this topology which has been verified using analytical and measured results are summarized below:

1) The measurement or the operating frequency is a stable fixed-point of the circuit and hence is robust to small perturbation and noise when compared to the open-loop configuration in Fig. 1(c).
2) The lock-in frequency is determined by the transducer impedance, hence, the measurement frequency need not be determined a-priori and the dynamic range of the converter is determined by the dynamic range of the relaxation oscillator.
3) The output of the proposed I-to-F converter is encoded as the frequency of a square-wave which can be viewed as a pulse-density digital code. Thus, the I-to-F converter does not need an additional analog-to-digital (ADC) converter. Even though this type of encoding is not minimal, simply using a counter or digital low-pass filter can estimate a binary encoding of the frequency measurement. The energy footprint for such a counter could be less than $1\,\mu$W for a counter operating at $100\,$kHz (assuming $1pJ/$bit operation).
4) The pulse-density digital code produced by the I-to-F converter can be used for direct frequency modulation which then be backscattered, similar to our previous approach [30]. This not only reduces the overall form-factor of the system but can significantly reduce the overall power-dissipation.
5) The fixed-point frequency F_{out} can be tuned such that when multiple sensors are used, the frequency output could be directly multiplexed over a single communication channel (wireless or wired). Combining the impedance sensing with the information multiplexing feature reduces the form factor, improves the energy-efficiency, and makes the proposed topology scalable across a large number of wearable sensors.

The paper is organized as follows: In Section II we first present a system-level analysis of the proposed impedance-to-frequency converter and highlight different design trade-offs. In Section III we present a circuit-level and system-level implementation of the converter, and in Section IV we present measurement results using an assembled prototype. Section V concludes the paper with a summary and comparison of system performance and a brief discussion of future directions.

II. I-to-F Converter Principle and Analysis

In this section, we describe the system-level architecture of the proposed I-to-F converter and analyze its system response. The architecture is shown in Fig. 2(a) where we have assumed that the transducer A is placed between two metallic junctions B and C. One junction B is connected to an external DC voltage source V_0 and the other junction C is used for sensing the load current I_L. To simplify the analysis we have assumed that the transducer equivalent circuit is a parallel combination of R_L and C_L. A combination of the bias current I_{ref} and a biasing resistor R_1 generates a change in the voltage V_x in response to the change in the load current I_L. A low-pass filter $H(s)$ tracks $\overline{V}_x$ which is the average of V_x. $\overline{V}_x$ then modulates the frequency F_{out} of the clock signal V_{CLK} generated by a voltage-controlled oscillator (VCO). V_{CLK} drives the switch M through an enable switch S. Note that the switch S is used to disable the feedback loop in which case the frequency

This article has been accepted for publication in IEEE Transactions on Biomedical Circuits and Systems. This is the author's version which has not been fully edited and content may change prior to final publication. Citation information: DOI 10.1109/TBCAS.2024.3362329

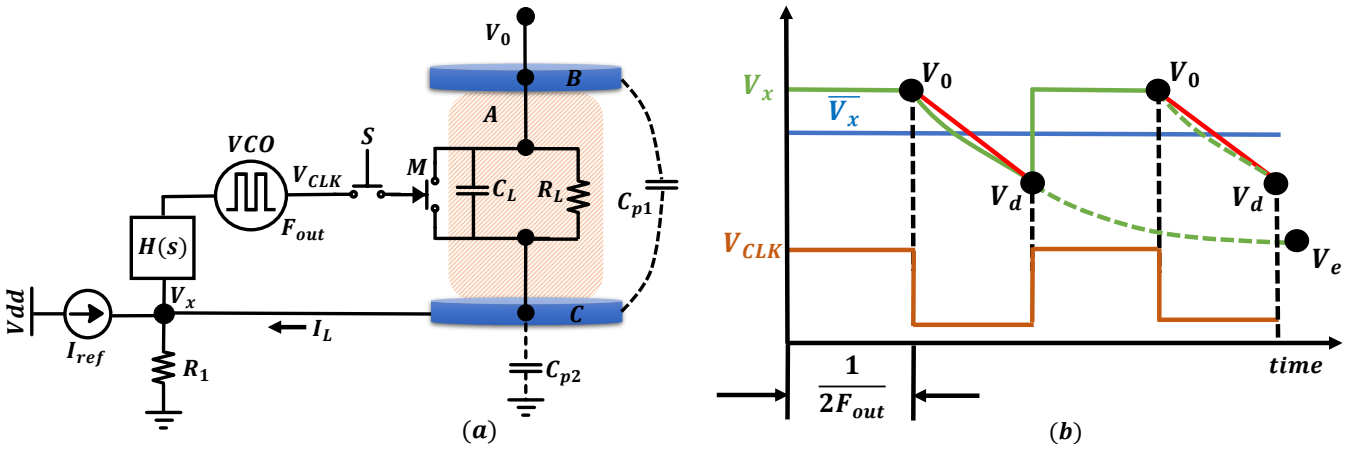

Fig. 2. (a) Equivalent circuit describing the operation of the proposed impedance-to-frequency converter; and (b) timing diagram showing the evolution of the voltage V_x when the switch S is ON and the VCO output drives the NMOS switch M. $\bar{V}_x$ shows an average of the voltage V_x and the red line represents a linear approximation to the Vx discharging curve.

F_{out} (in its steady state) is determined only by R_L. For the sake of completeness, in Fig. 2(a) we have also shown the parasitic capacitances C_{p1} and C_{p2} which will be ignored for the analysis below. We will assume a linear DC model for the VCO where F_{out} is related to its input voltage V_{in} according to

$$F_{out} = -\alpha V_{in} + \beta \tag{1}$$

where α and β are constant parameters. These coefficients will be determined experimentally as will be shown in Section III.

When the switch M is ON, the transducer is effectively short-circuited, hence the voltage $V_x = V_0$. When the switch M is OFF, the load current I_L is determined by both the current flowing through R_L and the discharge current through C_L. Applying Kirchhoff's current law (KCL) at node V_x leads to

$$I_{ref} + \frac{V_0 - V_x}{R_L} + C_L \frac{d(V_0 - V_x)}{dt} = \frac{V_x}{R_1} \tag{2}$$

which under steady-state (equilibrium) condition would let V_x converge to a potential V_e

$$V_e = \frac{V_0 R_1 + I_{ref} R_1 R_L}{R_1 + R_L}. \tag{3}$$

This is depicted in Fig. 2(b) which shows a timing diagram corresponding to the switch M which is periodically turned ON and OFF by V_{CLK} according to a frequency F_{out}. However, if $F_{out} >> 1/R_L C_L$, then we can linearize the differential equation 2 such that V_x discharges only to a non-equilibrium potential V_d, as shown in Fig 2. We have previously used non-equilibrium-based analysis for designing multi-channel data acquisition systems [21]. After linearization, as shown in Fig. 2, the equation 2 can be approximated as

$$I_{ref} R_L + V_0(1 + \frac{1}{\omega_1 T}) = V_d(1 + \frac{R_L}{R_1} + \frac{1}{\omega_1 T}) \tag{4}$$

where ω_1 & the sampling period T is given by

$$\omega_1 = \frac{1}{R_L C_L}, T = \frac{1}{2F_{out}} \tag{5}$$

A low-pass filter modeled as $H(s)$ in Fig.2(a) tracks the average voltage of V_x. Using the linearized equation 4 and assuming a 50% duty-cycle, we can estimate the average voltage $\overline{V_x}$ as

$$\overline{V_x} = \frac{3V_0 + V_d}{4} = \frac{V_0}{4}(3 + \frac{A}{B}) + \frac{I_{ref} R_L}{4B} \tag{6}$$

where,

$$A = 1 + \frac{1}{\omega_1 T} \tag{7}$$

$$B = 1 + \frac{R_L}{R_1} + \frac{1}{\omega_1 T}. \tag{8}$$

Fig. 2(b) shows the average voltage $\overline{V_x}$, which determines the VCO frequency F_{out} according to equation 1 as

$$\begin{aligned} F_{out} &= -\alpha \overline{V_x} + \beta \\ &= -(\frac{3}{4} + \frac{A}{4B})\alpha V_0 + \frac{\alpha}{4B} I_{ref} R_L + \beta \end{aligned} \tag{9}$$

Solving the equation 9 yields a quadratic problem in terms of locking frequency F_{out} of which only one is practically realizable and is given by the equation in table I. The equation shows that F_{out} and the dynamic range of the I-to-F converter can be adjusted by changing the current reference I_{ref} and V_0.

Figure 3(a) and (b) plot the value of F_{out} as the load resistance R_L and load capacitance C_L is varied. For each of these plots, the value of the external voltage source V_0 and I_{ref} are kept constant. The results show that F_{out} increases when R_L increases, whereas F_{out} decreases when C_L increases. This shows that the sensitivity of the I-to-F converter would match the physics of the sponge-transducer shown in Fig. 1 where the resistance and capacitance change in opposite direction in response to a mechanical stimulus [1]. The sensitivity of the I-to-F converter and the resulting signal-power can be estimated

TABLE I

$$F_{out} = \frac{2R_1(V_0\alpha - \beta) + \sqrt{(R_1+R_L)^2\omega_1^2 + \omega_1(R_1^2(2I_{ref}R_L\alpha - 4V_0\alpha + 4\beta) + 2R_1R_L(V_0\alpha - 2\beta)) + (2R_1V_0\alpha - 2\beta R_1)^2} - (R_1+R_L)\omega_1}{4R_1} \tag{10}$$

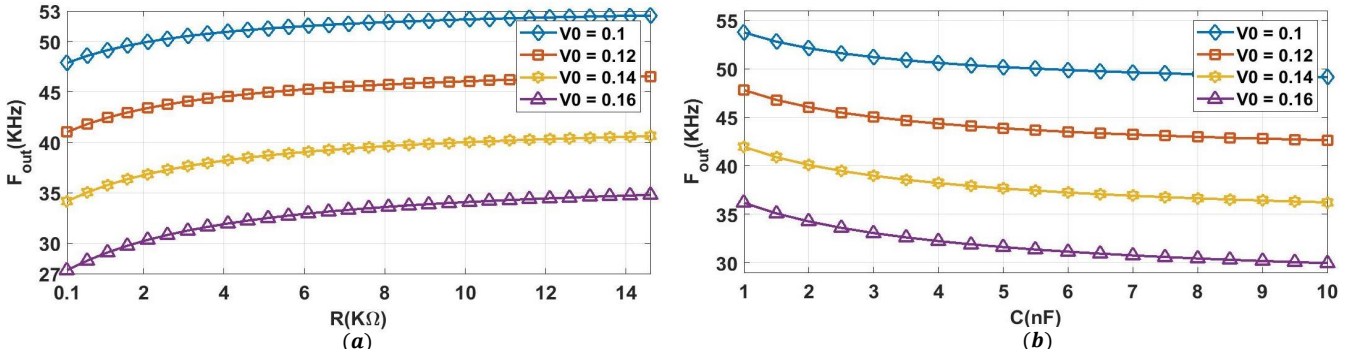

Fig. 3. Analytically calculated F_{out} for an RC parallel load with different R_L and C_L under 4 different V_0 external voltage sources and S ON modality: (a) For this transfer characteristics, R_L is varied, the capacitance C_L was chosen to be 1.5 nF. (b) For this transfer characteristics, C_L is varied, the resistance R_L was chosen to 14.67 kΩ.

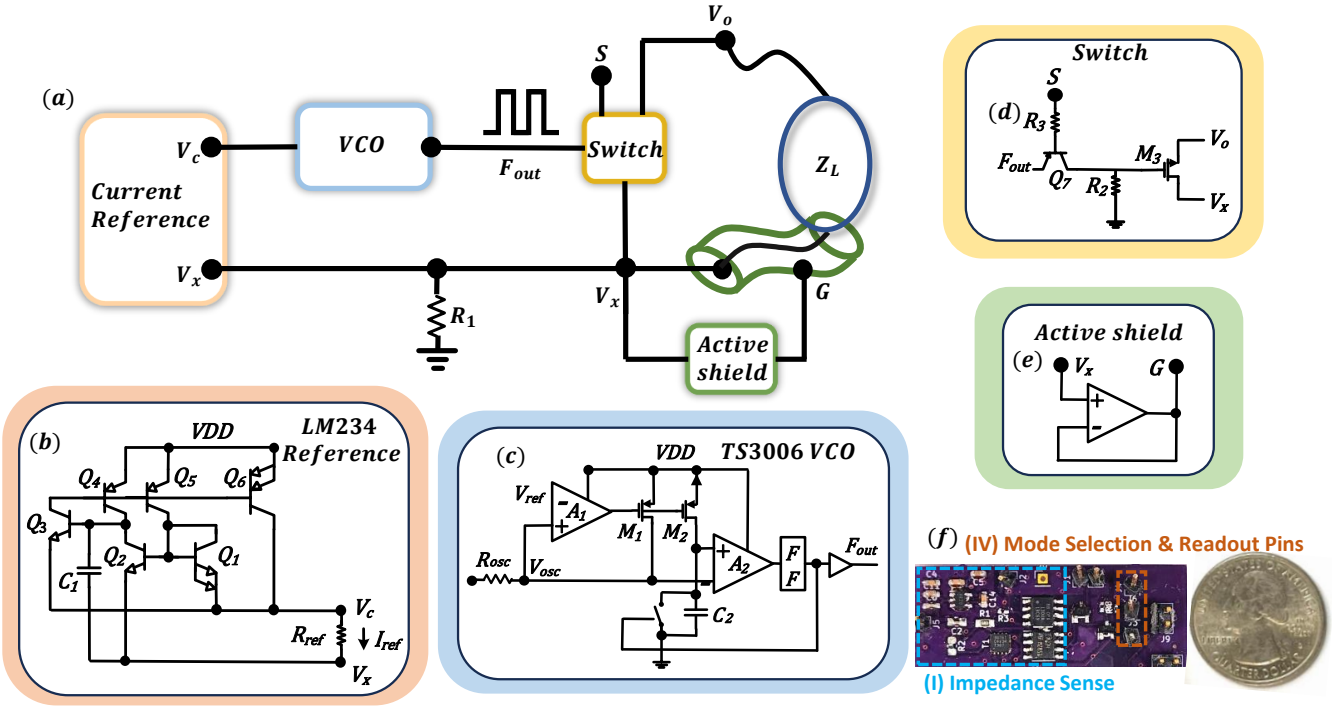

Fig. 4. (a) Circuit implementation of the proposed impedance-to-frequency converter comprising of (b) a current reference circuit, (c) a relaxation oscillator circuit, (d) a control switch, and (e) a circuit for active shielding. (f) Assembled printed circuit board(PCB) prototype of the converter using COTS chipsets.

through a perturbation analysis of F_{out} as

$$\Delta F_{out} = \frac{\partial F_{out}}{\partial R_L}\Delta R_L + \frac{\partial F_{out}}{\partial C_L}\Delta C_L \tag{11}$$

$$\Delta F_{out}^2 = \left(\frac{\partial F_{out}}{\partial R_L}\right)^2 \Delta R_L^2 + \left(\frac{\partial F_{out}}{\partial C_L}\right)\Delta C_L^2 + 2\left(\frac{\partial F_{out}}{\partial R_L}\right)\left(\frac{\partial F_{out}}{\partial C_L}\right)\Delta R_L\Delta C_L$$

where ΔR_L and ΔC_L denote incremental change in resistance and capacitance in response to mechanical deformation. The term ΔF_{out}^2 denotes the total signal-power and comprises of $\Delta R_L \Delta C_L$ which is the correlation between the resistance and capacitance change. Since $\Delta R_L \Delta C_L \leq 0$ for the sponge-transducer and from Fig. 1 and $\left(\frac{\partial F_{out}}{\partial R_L}\right)\left(\frac{\partial F_{out}}{\partial C_L}\right) \leq 0$ from Fig. 3, equation 11 indicate that the signal measured by the proposed I-to-F converter would be higher compared to measuring changes in R_L or C_L independently. This has been validated later in the measured results in section III. Note that

the variance/noise in measuring ΔF_{out} can be estimated as

$$\sigma^2\left(\Delta F_{out}\right) = \left(\frac{\partial F_{out}}{\partial R_L}\right)^2 \sigma^2\left(\Delta R_L\right) + \left(\frac{\partial F_{out}}{\partial C_L}\right)^2 \sigma^2\left(\Delta C_L\right) \tag{12}$$

where $\sigma^2\left(\Delta R_L\right)$ and $\sigma^2\left(\Delta C_L\right)$ denote the respective noise-power in measuring change in resistance and capacitance and are assumed to be independent.

To visualize the analysis based on equation 11, we consider the solution for F_{out} by restricting the operating regime to $1/\omega_1 T \gg R_L/R_1$ where the ratio $A/B \approx 1$ in equation 9. Note that this regime is achieved for large values of R_L or C_L. In this case F_{out} can be approximated as

$$F_{out} = \frac{\beta - \alpha V_0 + \sqrt{(\alpha V_0 - \beta)^2 + \frac{\alpha I_{ref}}{2C_L}}}{2} \tag{13}$$

which leads to

$$\frac{\partial F_{out}}{\partial R_L} = 0 \tag{14}$$

$$\frac{\partial F_{out}}{\partial C_L} = -\frac{\alpha I_{ref}}{8{C_L}^2\sqrt{(\alpha V_0 - \beta)^2 + \frac{\alpha I_{ref}}{2C_L}}} \tag{15}$$

Equation 14 shows that in this restricted regime the I-to-F converter is not sensitive to changes in resistance ΔR_L, however, the change in F_{out} is inversely proportional to change in ΔC_L. This operating regime highlights a key advantage of joint measurement of resistance and capacitance changes, compared to measuring just changes in resistance which might saturate at larger values.

Using equation 13 we can also derive the expression for input-referred noise in this restricted regime. We assume that the source of the external noise and variation is due to the parameters β and I_{ref} in equation 13 and the gain of the I-to-F is determined by gain α of the VCO. The input-referred noise (in-terms of voltage) is thus given by

$$\overline{{V_{in}}^2} = \frac{(\frac{\partial F_{out}}{\partial \beta})^2\sigma^2(\beta) + (\frac{\partial F_{out}}{\partial I_{ref}})^2\sigma^2(I_{ref})}{\alpha^2} \tag{16}$$

where,

$$\frac{\partial F_{out}}{\partial \beta} = \frac{1}{2}(1 - \frac{\alpha V_0 - \beta}{\sqrt{(\alpha V_0 - \beta)^2 + \frac{\alpha I_{ref}}{2C_L}}}) \tag{17}$$

$$\frac{\partial F_{out}}{\partial I_{ref}} = \frac{\alpha}{8C_L\sqrt{(\alpha V_0 - \beta)^2 + \frac{\alpha I_{ref}}{2C_L}}}. \tag{18}$$

The parameters $\sigma^2(\beta)$, $\sigma^2(I_{ref})$ denote the respective variance of β and I_{ref} and are determined by the circuit topology and the specific implementation of the I-to-F converter. In section III-A, we experimentally determine the magnitude of the input-referred noise.

A. I-to-F Circuit implementation

The system architecture shown in Fig. 2(a) has been implemented using the circuit shown in Figure 4(a). While each of the functional modules in Fig. 2(a) uses commercial-off-the-shelf (COTS) circuits the novelty lies in interfacing these circuits and exploiting the coupling between the circuits to optimize for energy-efficiency. For instance the current reference I_{Ref} implemented using a standard bipolar transistor-based PTAT circuit shown in Fig. 4(b) also implements the low-pass filter $H(s)$ in 4(a). I_{ref} is then determined by the resistor R_{ref} which sets the constant potential difference between the voltages V_c and $\overline{V}_x$. The VCO has been implemented using a standard relaxation oscillator, shown in Fig. 4(c) where the output frequency F_{out} is determined by the resistor R_{osc} and the voltage V_c. The switching circuit in the converter has been implemented using a combination of a bipolar and an nMOS transistor shown in Fig. 4(d). The circuit also includes an active shield module comprising of a buffer, as shown in Fig. 4(e), and is used to cancel out the parasitic capacitances C_{p1} and C_{p2} in Fig. 4(a). This ensures that the output frequency F_{out} is determined only by the load impedance Z_L. Fig. 4(f) shows an assembled impedance-to-frequency converter board that integrates different commercial-off-the-shelf (COTS) chipsets implementing each of the circuit modules in Fig. 4(b)-(e). While an integrated circuits approach would have led to significant miniaturization of the system, We chose a COTS approach because the form-factor of the overall system is limited by the size of the transducer and the battery. Furthermore, the COTS implementation of the PTAT, relaxation oscillator and the active shield are highly optimized for energy efficiency while achieving high reliability. In the prototype implementation, the PTAT current reference has been implemented using the LM234 chipset from Texas Instruments [31], the relaxation oscillator has been implemented using the TS3006 chipset from Silicon Lab [32]. Even though a COTS implementation was chosen to demonstrate the proof-of-concept, we note that a further improvement in energy-efficiency can be achieved using an integrated circuits (IC) implementation.

III. Measured Results

In this section we characterize the performance of the I-to-F converter circuit shown in Fig. 2 and verify the analysis presented in section II. In all experiments, the biasing current I_{ref} was chosen to be $9.4\mu A$ which sets an upper limit on the current flowing through the transducer impedance Z_L.

A. Model Characterization

Our initial measurements were designed to determine the VCO coefficients α and β in the equation 1 and to create a SPICE simulation model that could be used for parametric studies. Note that the VCO coefficients could have been estimated using an open-loop input-output measurement based on equation 1. However, equation 1 models the DC response of the VCO, whereas the circuit in Fig. 2 comprises of switching circuits and reactive elements in a feedback configuration. Therefore, a more accurate approach to estimate the coefficients α and β would be based on equation 9. Furthermore, the parameters of the low-pass filter $H(s)$ also needs to be estimated in the feedback configuration. In this experiment Z_L was fixed by choosing different values of R_L and C_L, and the voltage V_0 was swept. Estimation of

F_{out} was achieved by counting the number of digital cycles over a measurement window of 20 ms. Even though for this experiment a Keithley DAQ6510 data acquisition system [33] was used for frequency counting, any digital decimation filter implemented on a microcontroller or an FPGA could have been used.

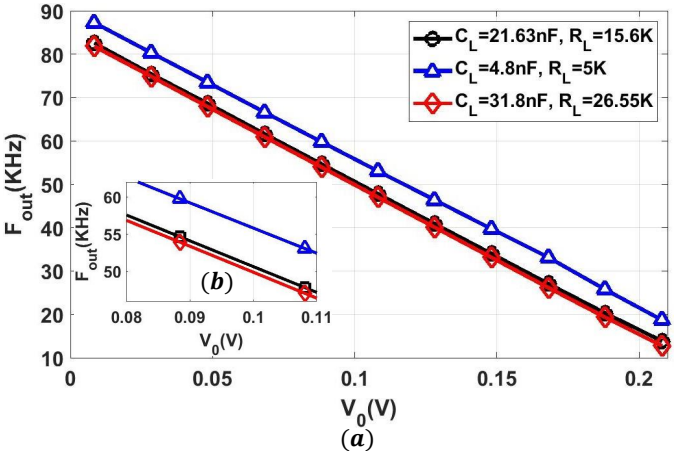

Fig. 5. (a) Measured transfer characteristic between the output frequency F_{out} and the tunable voltage V_0 for different values of R_L and C_L in Fig. 2. (b) A zoom-in of an arbitrary region to better visualize the output frequency difference.

V_0 was varied between 0.01 V to 0.21 V in increments of 0.02 V. Fig. 5 shows the measured results obtained for three different parallel RC combinations. The results conform to the linear model described by equation 9 and the VCO parameters are estimated to be $\alpha = 3.43 \times 10^5 Hz/V$ and $\beta = 8.2 \times 10^4 Hz$. These parameters have been used to validate the measured response in the subsequent experiments. Instead of directly estimating the parameters of the $H(s)$ in Fig.2(a), for the I-to-F SPICE model, we directly estimated the relationship between F_{out} and V_x using a fifth-order polynomial. A VerilogA model was used to implement the polynomial mapping in the SPICE simulations.

The next set of experiments used a parallel RC impedance to validate the analysis presented in section II. For the first experiment, R_L was varied from 130 Ω to 80 kΩ, whereas the capacitance C_L was held constant at 1.5 nF. Both the simulation and measured results are shown in Figure 6(a) which verifies the monotonic relationship between F_{out} and R_L consistent with the analysis in section II. Note that at higher value of R_L the sensitivity of F_{out} with respect to R_L decreases which confirms the model in equation 14. Higher sensitivity in F_{out} is achieved at lower values of R_L.

In the next set of experiments, R_L =14.67 kΩ was kept constant, whereas the capacitance C_L was varied from 1.5 nF to 22 nF. The simulation and measured results are shown in Figure 6(b), which shows the frequency F_{out} monotonically decreases with increase in C_L as described by the analysis in section II. Furthermore, the change in F_{out} is lower at higher values of C_L which is also consistent with the equation 15. The results in Figure 6 show that the SPICE model our modeled I-to-F converter simulation results match the measured results with the prototyped device.

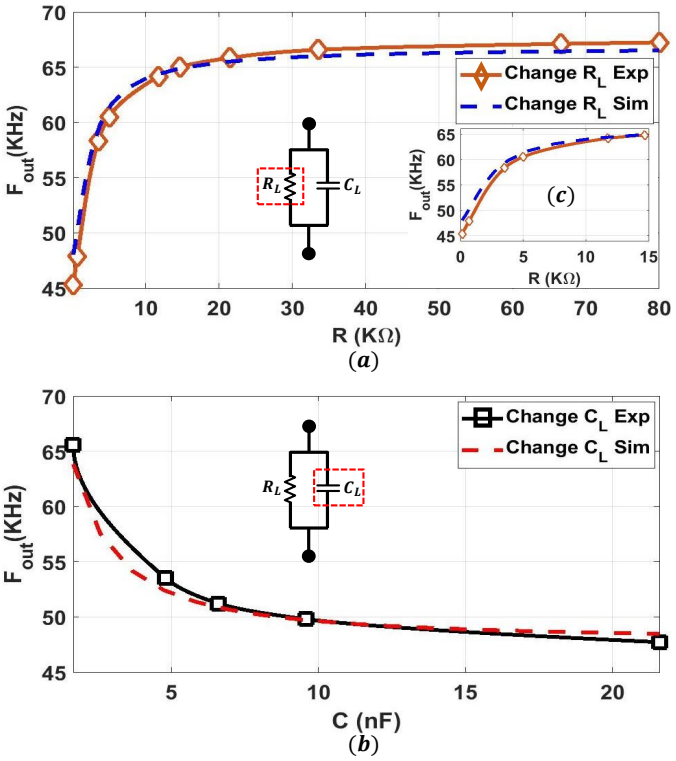

Fig. 6. Simulated and Measured F_{out} for an RC parallel load with different R_L and C_L when S is ON: (a) & (c) For this transfer characteristics R_L is varied, the capacitance C_L was chosen to be 1.5 nF. (b) For this transfer characteristics, C_L is varied, the resistance R_L was chosen to 14.67 kΩ

.

The next set of experiments verified the functionality of the I-to-F converter for different R-C impedance. One of the impedance corresponds to the equivalent circuit of the sponge transducer and comprises of the electrode resistance R_s in series with a parallel combination of R_L and C_L [1], shown in the inset of Fig.7(a) & (b). We first varied the series resistance R_s from 130 Ω to 80 kΩ, whereas R_L =14.67 kΩ and C_L =1.5 nF were kept constant. Then we kept the series resistance R_s = 5 kΩ and C_L =1.5 nF and varied R_L from 130 Ω to 80 kΩ. Both the simulation and measured results are shown in Fig.7(a) & (b). Next we verified the I-to-F converter response for an impedance comprising of a capacitance C_S in series with a parallel combination of R_L and C_L. We first varied the series capacitance C_s from C_s =1.5 nF to C_s =22 nF, while R_L =14.67 kΩ and C_L =1.5 nF were kept constant. Then we varied C_L from C_L =1.5 nF to C_L =22 nF, while keeping C_s =1.5 nF and R_L =14.67 kΩ constant. Fig.7(c) & (d) show both the measurement and simulation results, as well as the circuit model.

For estimating the input-referred noise of the I-to-F converter we followed the procedure described in [34]. A 3.5 kΩ and 1.5 nF parallel RC impedance was applied, and V_0 was set at 0.11 V. The frequency output of the voltage-controlled oscillator (VCO) was recorded using a Keithley DAQ6510, with a measurement window of 20 ms. The frequency output signal, with embedded noise, is depicted in Figure 8(a). To analyze the noise spectrum, we applied a Fast Fourier Transform (FFT) on the frequency output signal. In the previous experiment, we

This article has been accepted for publication in IEEE Transactions on Biomedical Circuits and Systems. This is the author's version which has not been fully edited and content may change prior to final publication. Citation information: DOI 10.1109/TBCAS.2024.3362329

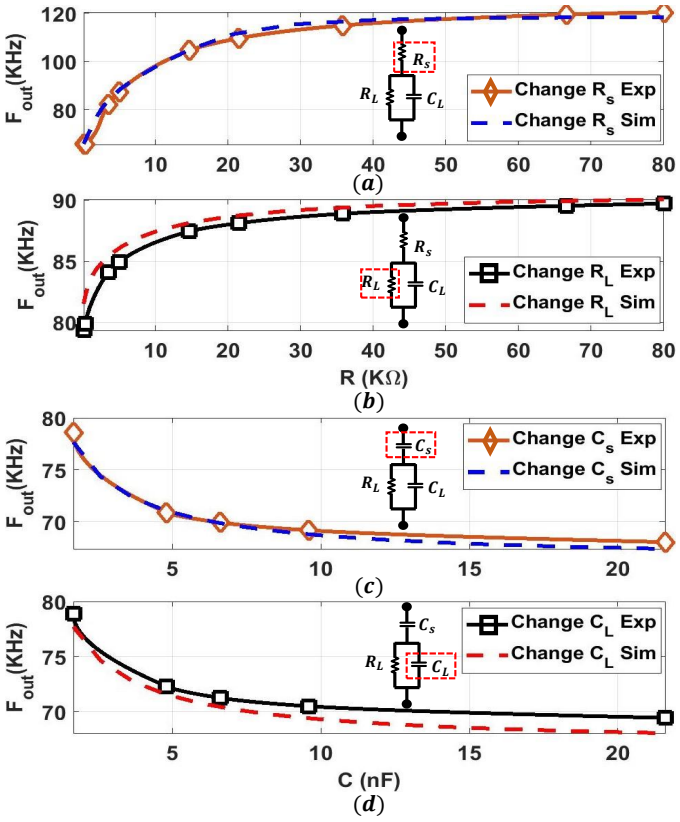

Fig. 7. Simulated and Measured F_{out} when S is ON and for different RC impedance shown in the inset: (a) F_{out} when series resistance R_s is varied, the capacitance C_L was chosen to be 1.5 nF and R_L was chosen to be 14.67 kΩ; (b) F_{out} when parallel resistance R_L is varied, the capacitance C_L was chosen to be 1.5 nF and R_s was chosen to be 5 kΩ; (c) F_{out} when series capacitance C_s is varied, the capacitance C_L was chosen to be 1.5 nF and R_L was chosen to be 14.67 kΩ; (d) F_{out} when capacitance C_L is varied, the capacitance C_s was chosen to be 1.5 nF and R_s was chosen to be 14.67 kΩ.

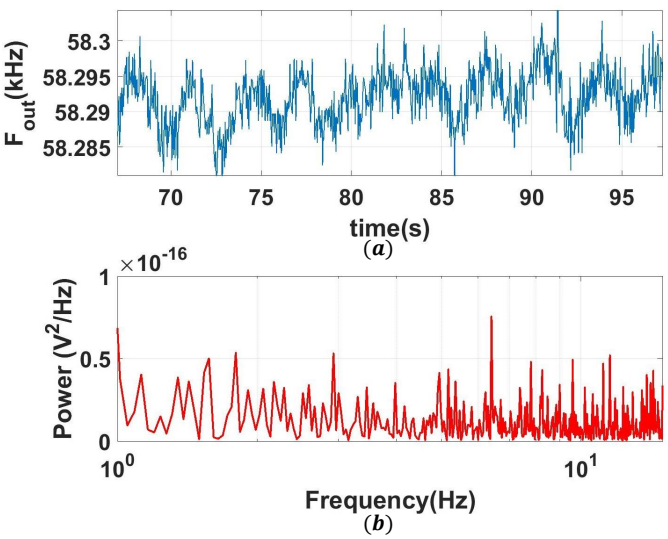

Fig. 8. (a) Measured frequency output under a 3.5 kΩ and 1.5 nF parallel RC impedance over a moving window of 20ms. (b) Power analysis plot of the measured frequency signal.

TABLE II
MEASURED SYSTEM SPECIFICATION

Parameter	Value
Supply Voltage	3.3 V
Current Consumption (Feedback off)	28 µA
Current Consumption (Feedback on)	128 µA
Voltage Controlled Oscillator	2.4 µA
Current Reference	9.8 µA
Switching Circuit	100 µA
Other Components	15.8 µA
Impedance Measurement Range	1-47 kΩ
Impedance Sensitivity @ $\|Z\| = 1.1$ kΩ	19.66 Hz/Ω
Impedance Sensitivity @ $\|Z\| = 47$ kΩ	0.05 Hz/Ω
Impedance Resolution @ $\|Z\| = 1.1$ kΩ	0.254Ω

derived the VCO parameter α, which allows the conversion of frequency output signal noise into input-referred voltage noise. The input-referred noise power is calculated and displayed in Figure 8(b) within a 15 Hz bandwidth. From this data, an estimated noise power of $0.5 \times 10^{-16} V^2/Hz$ can be inferred. Using the calculated noise power, the average input-referred noise is estimated to be approximately $7.07\,\mathrm{nV}/\sqrt{\mathrm{Hz}}$.

Table II summarizes the measured specifications of the I-to-F converter circuit shown in Figure 4. The Table includes a breakdown of the current consumed by each of the modules and the overall power dissipation (without the active shield circuit) of the converter. Note that the response of the I-to-F converter with respect to the magnitude of the impedance is non-linear. Therefore, the output sensitivity of the I-to-F converter is a function of its operating/biasing condition, and hence sensitivity is only defined for a small-signal operation. For the sensitivity measurements a parallel RC impedance was chosen with C =1.5 nF and R was varied from 3 kΩ to 4 kΩ. The frequency output changes from 58.32 kHz to 60.13 kHz, resulting in a calculated parallel RC impedance magnitude $|Z|$ varies from 1.13 kΩ to 1.224 kΩ. The sensitivity $\Delta F_{out}/\Delta|Z|$ is approximated as 19.66 Hz/Ω at $|Z| = 1.1$ kΩ. The I-to-F converter has a measured noise of approximately 5 Hz at the same operating point as shown in Figure 8(a). If we assume a system signal-to-noise ratio (SNR) of 1, the impedance resolution is approximated as 0.254 Ω.

The I-to-F converter's measurement range is defined as the range of the impedance magnitude $|Z|$ over which the measured sensitivity is at least 0.05 Hz/Ω. To estimate the measurement range, we biased the parallel RC load at C =15 pF and R was varied from 99 kΩ to 100 kΩ. The frequency output varies from 118.26 kHz to 118.27 kHz, corresponding to a impedance magnitude $|Z|$ change from 47.1 kΩ to 47.3 kΩ.

B. Radial Pulse Sensing

The objective of this experiment was to verify the higher sensitivity of the proposed I-to-F converter for monitoring the radial artery pulse. We recreated the experimental setup that

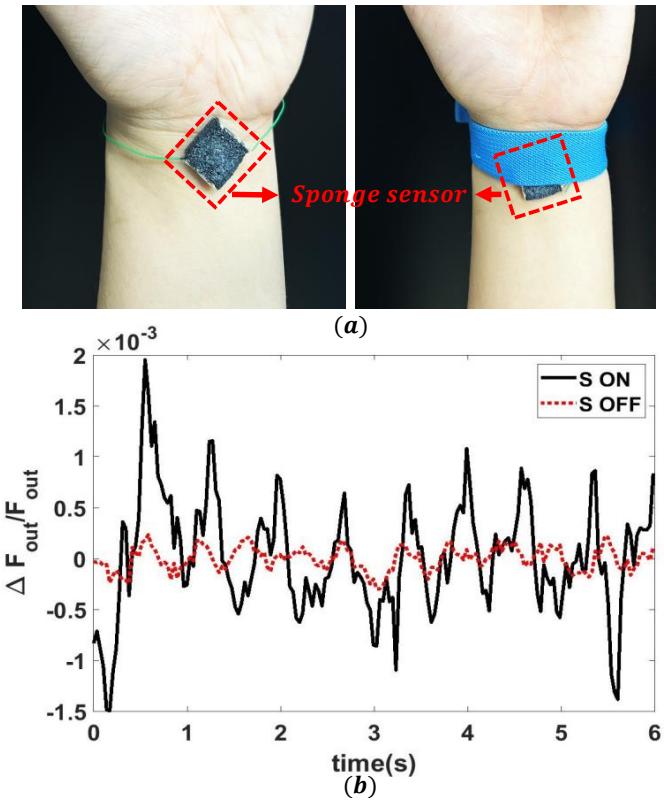

Fig. 9. Measured radial pulse sensing results using a prototype sponge transducer: (a) experimental setup where the transducer is clamped to the wrist; and (b) measured normalized temporal changes in the converter frequency $\boldsymbol{\Delta F_{out}/F_{out}}$ for $\boldsymbol{S}$-ON mode and $\boldsymbol{S}$-OFF mode respectively.

was reported in [12] and shown in Fig. 9(a) where the I-to-F converter was interfaced with a sponge transducer. The transducer was fabricated using porous polydimethylsiloxane (PDMS) cubes coated with a conductive polymer PEDOT:PSS. Details regarding the fabrication of the transducer and its electrical characterization can be found in our previous work [1] and has been omitted here for the sake of brevity. To ensure stable recording, a wristband was wrapped over the sensor, providing secure and consistent contact. The mechanical changes induced by arterial pulses was sensed by the sponge transducer as a change in impedance which was then measured by the I-to-F converter. Each experiment was repeated twice where the I-to-F converter was set to S-ON and S-OFF modes. Figure 9(b) shows the measured results for both the modes, where we have plotted only the change in ΔF_{out} from the baseline frequency. The measured results clearly show the arterial pulse signal corresponding to a heart rate of 108 beats per minute (bpm). However, the higher sensitivity of I-to-F converter in S-ON mode can be clearly seen when compared to the I-to-F converter output in S-OFF mode. This improvement in sensitivity allows for more accurate and reliable detection of the radial pulse signals.

C. Gesture Tracking Application

The next set of experiments explored the use of the sponge-transducer and the I-to-F converter for gesture-tracking application. The specific gesture that was chosen was the mechanical motion of the human finger. In Figure 10(a) we show the placement of the sponge transducer on a human finger joint in a straight and a bent position respectively. In the straight position, the sponge sensor maintains its original shape, whereas bending the finger causes the transducer to stretch, resulting in a change in the transducer's impedance. These impedance changes are measured by the I-to-F converter. The states of the finger (bent and unbent) was maintained for a duration of 5-seconds and the measured responses are shown in Figure 10(b). For comparison, the response of the I-to-F converter is measured for the modes S-ON and S-OFF. The measured results clearly show higher sensitivity in the S-ON mode when both R_L and C_L are being sensed. Note that in Figure 10(b) the waveforms corresponding to S-ON and S-OFF are not time-aligned as the experiments were conducted independently. Figure 10(b) shows more than 10 times higher sensitivity when compared to measuring changes in resistance.

D. Multi-sensor experiment & Frequency-multiplexing

Since the baseline frequency of the converter can be set using the voltage V_0, it is possible to set the baseline operating frequency F_{out} of many I-to-F converters to be different. This enables frequency-multiplexing of the sensed information (encoded by ΔF_{out}) over a common physical channel (Wireless, wired or using the body-channel) [35]–[38]. In the next set of experiments we have verified the frequency multiplexing measurement using an experimental setup shown in Fig 10(c). Two sponge-transducers and I-to-F converters were attached to different fingers and their outputs F_{out} were physically connected to each other using a piece of wire. The transmission bandwidth is set by the VCO output frequency range, which is determined by resistor R_{osc}, as explained in II-A. We chose R_{osc} to be $1\,\mathrm{M\Omega}$, achieving a bandwidth of $108\,\mathrm{kHz}$.

The external voltage sources V_0 were set to $0.11\,\mathrm{V}$ and $0.24\,\mathrm{V}$ to bias the output frequency baseline at $85\,\mathrm{kHz}$ and $60\,\mathrm{kHz}$, respectively. The measured results are shown in Fig 10(d), which shows that different hand-motions corresponding to different finger movements (clicking the mouse).

Fig 10(d), shows the time-frequency measurement where one can clearly distinguish the two types of motions, shown in Fig 10(c). The multiplexed time-frequency waves were then separated into two sections based on a $70\,\mathrm{kHz}$ cutoff frequency. Note that previous work [1] has shown that for the sponge transducer, the resistance and capacitance change differently in response to compressive strain, tensile strain, and pressure. This attribute in conjunction with the proposed impedance-to-frequency conversion could therefore be used for designing multi-modal and frequency multiplexed sensors.

IV. Conclusions and Discussions

This paper presents a compact, impedance-to-frequency (I-to-F) converter that is suitable for integration with a multi-modal transducer that changes its impedance in response to mechanical deformation. By simultaneously monitoring the changes in resistance and capacitance across a sponge-based

This article has been accepted for publication in IEEE Transactions on Biomedical Circuits and Systems. This is the author's version which has not been fully edited and content may change prior to final publication. Citation information: DOI 10.1109/TBCAS.2024.3362329

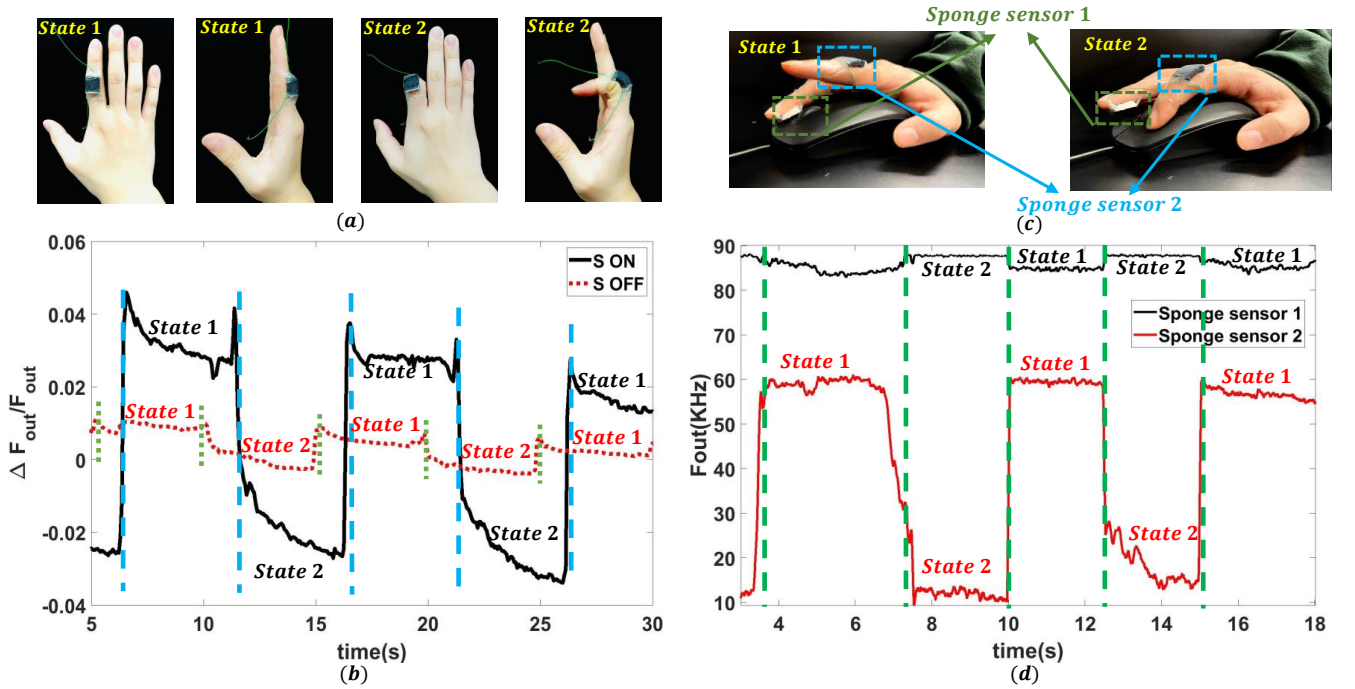

Fig. 10. Experiment to validate the application of the converter for gesture tracking and the multi-access capability of the impedance-to-frequency converter: (a) measurement setup showing the sponge transducer attached to a human finger joint when the finger is straight (state 1) and when the finger is bent at 90 degrees (state 2); (b) measured the normalized ΔF_{out} dynamics ($\Delta F_{out}/F_{out}$) when switching between state 1 and state 2, shown here for resistance only sensing mode and impedance sensing mode; (c) experimental setup comprising of two sponge transducers/converters (sensor 1 and 2) in two different states (state1 and state2); (d) Measured output after signal demultiplexing which clearly shows the dynamic states of both sensors.

TABLE III
PERFORMANCE COMPARISION

Parameter	This work	Zamani [39]	Yan [40]	Kim [41]	AFE4300 [42]
Supply Voltage	3.3	1	1.8	0.5	3
Modulation	Square	Semi-ramp	Square	Pseudo-sine	Pseudo-sine
Injection Current	$< 10\,\mu A$	0.5-1 µA	10-40 µA	8.4 µA	NA
Injection frequency	NA	2 kHz	2 kHz	20/50 Hz	8/16/3264 Hz
Measurement Range	1 to 47 kΩ	0.1 to 3.3 kΩ	0.1 to 4.4 kΩ	NA	NA
Input-referred noise	$7.07\,nV/\sqrt{Hz}$	$221.36\,nV/\sqrt{Hz}$	$146.46\,nV/\sqrt{Hz}$	$45\,nV/\sqrt{Hz}$	$48\,nV/\sqrt{Hz}$
Supply Current	128 µA	1.55 µA	28 µA	18.5 µA	970 µA

multi-modal transducer, the proposed I-to-F converter was shown to exhibit significantly higher sensitivity compared to monitoring just the change in resistance. Even though the functionality of the proposed I-to-F converter has been demonstrated for the sponge-sensor, the converter can be used for other types of transducers. For specific impedance configuration combination, as shown in Fig.7(a), the functionality of the I-to-F converter can be augmented to determine the resistive and the capacitive components of the impedance. This is achieved by enabling and disabling the feedback using the external switch S in Fig. 2. When S is turned ON, the I-to-F measures the magnitude of the impedance, whereas when the S is turned OFF, the I-to-F measures only the resistance. Using the two-point measurements (in the ON and OFF states) the I-to-F could therefore be used to estimate both the resistive and reactive components.

Since the proposed I-to-F converter uses a fixed-point approach for measuring impedance, the process eliminates the need for sinusoidal current source generation, signal amplification and analog-to-digital conversion stages. This makes the architecture simple and amenable for a ultra-low-power implementation. Even though a COTS approach have been used for proof-of-concept, the architecture can be easily mapped onto an integrated circuits solution. This will lead to further miniaturization and improvements in energy-efficiency. However, even with a COTS implementation, the proposed I-to-F converter achieve better performance metrics when compared to other impedance measurement solutions reported

in literature as shown in the Table III. Notably, most of the solutions examined utilize a conventional topology, as depicted in Figure 1(c). In contrast, our approach, based on commercial off-the-shelf (COTS) components, leverages a novel topology as proposed in Figure 1(d). It's important to highlight that the solutions discussed in [39]–[42] primarily encompass analog front-ends, typically requiring a separate analog-to-digital converter (ADC) for integration into a complete system. Our prototype uniquely integrates the ADC functionality.

The custom integrated circuit solutions highlighted in [39]–[41] are reported in academic literature and while these solutions exhibit lower current consumption, they often compromise important performance factors such as dynamic range and input-referred noise. In comparison, our COTS-based solution is more directly comparable to the widely used commercial product, the Texas Instruments AFE4300. Notably, our system outperforms the AFE4300 in various key performance metrics, as evident from the comparison table. The commercial-off-the-shelf (COTS) chipsets are generally trimmed to be robust to mismatch. However, the converter architecture will exhibit sensitivity to ambient temperature. The oscillator's temperature dependency coefficient is reported as $0.02\%/°C$ [32], which shows a minimal effect on the parameter β in equation1. The highest sensitivity to temperature variation arises due to the PTAT current reference. For LM234 reference, the reported temperature dependence is $0.33\%/°C$ [31] which results in a 0.195% change in the output frequency for a $1°C$ variation in temperature.

In addition to measuring changes in impedance, we also demonstrated that the I-to-F converter can support frequency multiplexing of the measured output where many converters can be connected to the same physical communication channel. This feature makes the design scalable to a large number of transducers. We can configure system parameters to ensure that different I-to-F converters operate within different frequency bands. The frequency range of the I-to-F converter can be adjusted by tuning the current reference I_{ref} and the center frequency can be adjusted by changing the external voltage source V_0. Future work will entail dynamic adjustment of I_{ref} and V_0 such that the performance of the I-to-F converter can be optimized.

REFERENCES

[1] L.-W. Lo, J. Zhao, H. Wan, Y. Wang, S. Chakrabartty, and C. Wang, "A soft sponge sensor for multimodal sensing and distinguishing of pressure, strain, and temperature," *ACS Applied Materials & Interfaces*, vol. 14, no. 7, pp. 9570–9578, 2022.

[2] L.-W. Lo, J. Zhao, K. Aono, W. Li, Z. Wen, S. Pizzella, Y. Wang, S. Chakrabartty, and C. Wang, "Stretchable sponge electrodes for long-term and motion-artifact-tolerant recording of high-quality electrophysiologic signals" *ACS Nano*, vol. 16, no. 8, pp. 11792–11801, 2022.

[3] B. Paolo, "Wearable sensors/systems and their impact on biomedical engineering," *IEEE Engineering in Medicine and Biology Magazine*, vol. 22, pp. 18–20, 2003.

[4] L.-W. Lo, J. Zhao, H. Wan, Y. Wang, S. Chakrabartty, and C. Wang, "An inkjet-printed pedot:pss-based stretchable conductor for wearable health monitoring device applications," *ACS Applied Materials & Interfaces*, vol. 13, no. 18, pp. 21 693–21 702, 2021.

[5] C. Pang, C. Lee, and K.-Y. Suh, "Recent advances in flexible sensors for wearable and implantable devices," *Journal of Applied Polymer Science*, vol. 130, pp. 1429–1441, 2013.

[6] T. Kuniharu, H. Wataru, H. Shingo, A. Takayuki, and A. Seiji, "Toward flexible and wearable human-interactive health-monitoring devices," *Advanced Healthcare Materials*, vol. 4, pp. 487–500, 2014.

[7] H. Wan, J. Zhao, L.-W. Lo, Y. Cao, N. Sepúlveda, and C. Wang, "Multimodal artificial neurological sensory–memory system based on flexible carbon nanotube synaptic transistor," *ACS Nano*, vol. 15, no. 9, pp. 14587–14597, 2021.

[8] H. Wan, Y. Cao, L.-W. Lo, J. Zhao, N. Sepúlveda, and C. Wang, "Flexible carbon nanotube synaptic transistor for neurological electronic skin applications," *ACS Nano*, vol. 14, no. 8, pp. 10402–10412, 2020.

[9] S. C. Mukhopadhyay, "Wearable sensors for human activity monitoring: A review," *IEEE Sensors Journal*, vol. 15, no. 3, pp. 1321–1330, 2014.

[10] J. Kim, M. Kim, M.-S. Lee, K. Kim, S. Ji, Y.-T. Kim, J. Park, K. Na, K.-H. Bae, H. K. Kim, F. Bien, C. Y. Lee, and J.-U. Park, "Wearable smart sensor systems integrated on soft contact lenses for wireless ocular diagnostics," *Nature Communications*, vol. 8, no. 14997, 2017.

[11] S. Liu, J. Zhang, Y. Zhang, and R. Zhu, "A wearable motion capture device able to detect dynamic motion of human limbs," *Nature Communications*, vol. 11, no. 5615, 2020.

[12] L.-W. Lo, H. Shi, H. Wan, Z. Xu, X. Tan, and C. Wang, "Inkjet-printed soft resistive pressure sensor patch for wearable electronics applications," *Advanced Materials Technologies*, vol. 5, 1900717, 2019.

[13] B. Ketelsen, M. Yesilmen, H. Schlicke, H. Noei, C.-H. Su, Y.-C. Liao, and T. Vossmeyer, "Fabrication of strain gauges via contact printing: A simple route to healthcare sensors based on cross-linked gold nanoparticles," *ACS Applied Materials & Interfaces*, vol. 10, no. 43, pp. 37 374–37 385, 2018.

[14] H. Souri, H. Banerjee, A. Jusufi, N. Radacsi, A. A. Stokes, I. Park, M. Sitti, and M. Amjadi, "Wearable and stretchable strain sensors: Materials, sensing mechanisms, and applications," *Advanced Intelligence Systems*, vol. 2, no. 2000039, 2020.

[15] J. Chen, J. Zheng, Q. Gao, J. Zhang, J. Zhang, O. M. Omisore, L. Wang, and H. Li, "Polydimethylsiloxane (PDMS)-based flexible resistive strain sensors for wearable applications," *Applied Sciences*, vol. 8, no. 3, p. 345, 2018.

[16] M. Amjadi, K.-U. Kyung, I. Park, and M. Sitti, "Stretchable, skin-mountable, and wearable strain sensors and their potential applications: A review," *Advanced Functional Materials*, vol. 26, pp. 1678–1698, 2016.

[17] C. Pang, G.-Y. Lee, T. il Kim, S. M. Kim, H. N. Kim, S.-H. Ahn, and K.-Y. Suh, "A flexible and highly sensitive strain-gauge sensor using reversible interlocking of nanofibres," *Nature Materials*, vol. 11, pp. 795–801, 2012.

[18] A. Paul, M. S. Lee, Y. Xu, S. R. Deiss, and G. Cauwenberghs, "A versatile in-ear biosensing system and body-area network for unobtrusive continuous health monitoring," *IEEE Transactions on Biomedical Circuits and Systems*, vol. 17, no. 3, pp. 483–494, 2023.

[19] Y. M. Chi, Y.-T. Wang, Y. Wang, C. Maier, T.-P. Jung, and G. Cauwenberghs, "Dry and noncontact EEG sensors for mobile brain–computer interfaces," *IEEE Transactions on Neural Systems and Rehabilitation Engineering*, vol. 20, no. 2, pp. 228–235, 2012.

[20] C.-C. Chung, D. Sheng, and M.-H. Li, "Design of a human body channel communication transceiver using convolutional codes," *Microelectronics Journal*, vol. 100, p. 104783, 2020.

[21] W. Li, Z. Xiao, J. Zhao, K. Aono, S. Pizzella, Z. Wen, Y. Wang, C. Wang, and S. Chakrabartty, "A portable and a scalable multi-channel wireless recording system for wearable electromyometrial imaging," *IEEE Transactions on Biomedical Circuits and Systems*, vol. 17, no. 5, pp. 916–927, 2023.

[22] L. Roberts,"The evolution of packet switching," *Proceedings of the IEEE*, vol. 66, pp. 1307 – 1313, 1978.

[23] J. W. Atkins, N. J. P. Cooper, and K. E. Gleen, "The evolving art of packet switching," *BT Technology Journal*, vol. 25, pp. 222–228, 2007.

[24] Z. Haas and D. Cheriton, "Blazenet: a packet-switched wide-area network with photonic data path," *IEEE Transactions on Communications*, vol. 38, pp. 818–829, 1990.

[25] M. Jung, K. koong, Y. Lee, Y. Koh, K. Eom, H. Jang, W. Jung, J. Bae, and J. Park, "Wrist-wearable bioelectrical impedance analyzer with miniature electrodes for daily obesity management," *Scientific Reports*, vol. 11, no. 1238, 2020.

[26] M. Usman, M. Leone, A. K. Gupta, and W. Xue, " Fabrication and analysis of wearable bioimpedance analyzers on paper and plastic substrates," *IEEE Sensors Letters*, vol. 4, no. 3, 2020.

[27] P. Kassanos, F. Seichepine, and G.-Z. Yang, "A comparison of front-end amplifiers for tetrapolar bioimpedance measurements," *IEEE Transactions on Instrumentation and Measurement*, vol. 70, 2020.

[28] J. Torrents and R. Pallas-Areny, "Compensation of impedance meters, when using an external front-end amplifier," *IEEE Transactions on Instrumentation and Measurement*, vol. 51, no. 2, pp. 310–313, 2002.
[29] Y. Wu, F. F. Hanzaee, D. Jiang, R. H. Bayford, and A. Demosthenous, "Electrical impedance tomography for biomedical applications: Circuits and systems review," *IEEE Open Journal of Circuits and Systems*, vol. 2, pp. 380–397, 2021.
[30] Y. Alazzawi, K. Aono, E. L. Scheller, and S. Chakrabartty, "Exploiting self-capacitances for wireless power transfer," *IEEE Transactions on Biomedical Circuits and Systems*, vol. 13, no. 2, pp. 425–434, 2019.
[31] Texas intruments, "LM134/LM234/LM334 3-Terminal adjustable current sources"[Online].Available:https//www.ti.com/lit/ds/symlink/lm234.pdf.
[32] Silicon Labs, "A 1.55V to 5.25V, 1.9µA, 9kHz to 300kHz silicon timer." [Online].Available:https://www.mouser.com/datasheet/2/472/TS3006-2508300.pdf
[33] Tektronix "DAQ6510 data acquisition and logging, Multimeter System." [Online].Available:https://download.tek.com/datasheet/1KW-613170DAQ6510Datasheet020321.pdf.
[34] M. Zamani, Y. Rezaeiyan, O. Shoaei, and W. A. Serdijn, "A 1.55µW bio-impedance measurement system for implantable cardiac pacemakers in 0.18µm CMOS," *IEEE Transactions on Biomedical Circuits and Systems*, vol. 12, no. 1, pp. 211–221, 2018.
[35] L. P, M. I. Wani, S. S. Khan, and S. Malik, "Autonulling-based multichannel impedance measurement system for capacitive sensors," *IEEE Sensors Letters*, vol. 7, no. 3, pp. 1–4, 2023.
[36] C. A. Delianides, S. Pourang, P. Mohseni, and M. A. Suster, 'A multichannel miniaturized dielectric blood coagulometer for point-of-care assessment of hemostasis," in *2022 IEEE Biomedical Circuits and Systems Conference (BioCAS)*, 2022, pp. 188–192.
[37] M. ElAnsary, N. Soltani, H. Kassiri, R. Machado, S. Dufour, P. L. Carlen, M. Thompson, and R. Genov, "50nW opamp-less $\Delta\Sigma$ -modulated bioimpedance spectrum analyzer for electrochemical brain interfacing," *IEEE Journal of Solid-State Circuits*, vol. 55, no. 7, pp. 1971–1983, 2020.
[38] J. Ojarand, M. Min, and A. Koel, "Multichannel electrical impedance spectroscopy analyzer with microfluidic," *Sensors*, vol. 19, no. 8, p. 1891, 2019.
[39] M. Zamani, Y. Rezaeiyan, O. Shoaei, and W. A. Serdijn, "A 1.55 µW bio-impedance measurement system for implantable cardiac pacemakers in 0.18 µm CMOS," *IEEE Transactions on Biomedical Circuits and Systems*, vol. 12, no. 1, pp. 211–221, 2018.
[40] L. Yan, J. Pettine, S. Mitra, S. Kim, D.-W. Jee, H. Kim, M. Osawa, Y. Harada, K. Tamiya, C. Van Hoof, and R. F. Yazicioglu, "A 13 µA analog signal processing IC for accurate recognition of multiple intra-cardiac signals," *IEEE Transactions on Biomedical Circuits and Systems*, vol. 7, no. 6, pp. 785–795, 2013.
[41] K. Kim, J.-H. Kim, S. Gweon, J. Lee, M. Kim, Y. Lee, S. Kim, and H.-J. Yoo, "22.3 A 0.5V 9.26µW 15.28mΩ/Hz bio-impedance sensor IC with 0.55° overall phase error," in *2019 IEEE International Solid- State Circuits Conference - (ISSCC)*, pp. 364–366.
[42] Texas Intruments, "AFE4300 low-cost, integrated analog front-end for weight-scale and body composition measuremen," 2019. [Online]. Available:https://www.ti.com/lit/ds/symlink/afe4300.pdf.

Weilun Li is a Ph.D. candidate in Electrical and Systems Engineering at Washington University in Saint Louis, Saint Louis, MO, USA. He received an M.S. degree in Electrical Engineering from the University of Pennsylvania, Philadelphia, PA, USA, in 2021. He received a B.S. degree in physics from Dickinson College, Carlisle, PA, USA, in 2019. In 2020 he worked as an Electrical Engineering Intern at Wyatt Technology in Santa Barbara, CA, USA. He is an IEEE student member. His current research interests include biopotential recording instrumentation design, neural amplifiers, brain-machine interfaces, wearable health monitoring systems, and portable ECG monitoring.

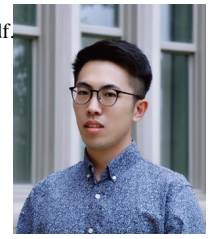

Junyi Zhao received the B.S. degree in Mechanical Engineering from Huazhong University in Science and Technology (HUST), Wuhan, China, in 2019. He is currently a Ph.D. candidate in Electrical Engineering at Washington University in St. Louis (WUSTL), MO, USA. From 2017 to 2019, he was an undergraduate researcher in State key Lab of Digital Manufacturing Equipment & Technology, Hubei, China, focusing on the microfabrication of flexible and stretchable electronics. In 2018, he visited University of Houston (UH), Texas, USA, as a research assistant studying laser-driven microfluidics. Since 2019, he has been working as a Ph.D. researcher in WUSTL, mainly focusing on intrinsically flexible/stretchable optoelectronic devices and wearable electronics.

Yong Wang (M'2020) received the B.S. and M.S. degrees in electrical engineering from Xi'an Jiaotong University, Xi'an, China in 1999 and 2022 respectively. In 2009, he received the Ph.D. degree in Biomedical engineering from Washington University in St. Louis. From 2009 to 2013, he was a postdoc research associate at Mallinckrodt Institute of Radiology at Washington University in St. Louis, School of Medicine. From 2013 to 2015, he was a research instructor at Mallinckrodt Institute of Radiology. From 2015 to 2020, he was an assistant professor at the Obstetrics and Gynecology Department at Washington University in St. Louis, School of Medicine. Since 2020, He has been an associate professor with tenure in the departments of Obstetrics and Gynecology and electrical and systems engineering at Washington University in St. Louis. His research interests include medical imaging system development, image processing, inverse problems, electrophysiological imaging system, and magnetic resonance imaging.

Chuan Wang is an assistant professor of Electrical & Systems Engineering at Washington University in St. Louis. Prior to that, he was an assistant professor of Electrical & Computer Engineering at Michigan State University from 2013 to 2018. He received a B.S. in Microelectronics from Peking University in 2005 and a Ph.D. in Electrical Engineering from the University of Southern California in 2011. From 2011 to 2013, he worked as a postdoctoral scholar in the Department of Electrical Engineering and Computer Sciences at the University of California, Berkeley.

Prof. Wang's research interests include flexible/stretchable electronics and printed electronics for sensing, displaying, and energy harvesting applications, as well as emerging semiconductor materials for nanoelectronic and optoelectronic devices.

This article has been accepted for publication in IEEE Transactions on Biomedical Circuits and Systems. This is the author's version which has not been fully edited and content may change prior to final publication. Citation information: DOI 10.1109/TBCAS.2024.3362329

Shantanu Chakrabartty (S'99-M'04-SM'09) received his B.Tech degree from the Indian Institute of Technology, Delhi in 1996, M.S and Ph.D. degrees in Electrical Engineering from Johns Hopkins University, Baltimore, MD, USA in 2002, and 2004 respectively. From 1996 to 1999, he was with Qualcomm Inc., San Diego, CA, USA. From 2004 to 2015, he was an Associate Professor with the Department of Electrical and Computer Engineering, Michigan State University (MSU), MI, USA. He is currently a Clifford W. Murphy Professor and the Vice-Dean for Research and Graduate Education at McKelvey School of Engineering at Washington University in St. Louis, MO, USA. Dr. Chakrabartty was a Catalyst Foundation fellow from 1999-2004 and is a recipient of the National Science Foundation's CAREER award, the University Teacher-Scholar Award from MSU, and the 2012 Technology of the Year Award from MSU Technologies. Dr. Chakrabartty is a fellow of the American Institute of Medical and he has previously served as the associate editor for IEEE Transactions of Biomedical Circuits and Systems.